LANGMUIR

pubsiacs.org/Langmuir Article

New Insights into the Formation of Aggregates of Bidisperse Nanoand Microplastics in Water Based on the Analysis of In Situ Microscopy and Molecular Simulation

Christian Bentum Hammond, Abolfazl Faeli Qadikolae, Mohammadreza Aghaaminiha, Sumit Sharma, and Lei Wu*



Cite This: Langmuir 2024, 40, 14455-14466



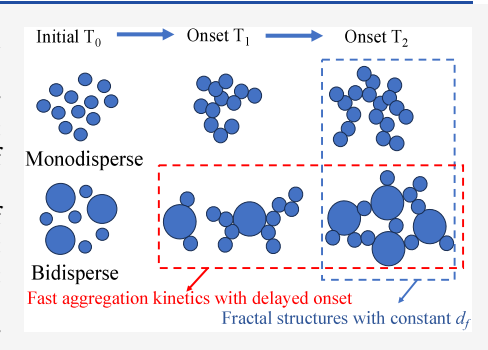
ACCESS I

III Metrics & More

Article Recommendations

Supporting Information

ABSTRACT: Microplastics (MPs) and nanoplastics (NPs) in water pose a global threat to human health and the environment. To develop efficient removal strategies, it is crucial to understand how these particles behave as they aggregate. However, our knowledge of the process of aggregate formation from primary particles of different sizes is limited. In this study, we analyzed the growth kinetics and structures of aggregates formed by polystyrene MPs in mono- and bidisperse systems using in situ microscopy and image analysis. Our findings show that the scaling behavior of aggregate growth remains unaffected by the primary particle size distribution, but it does delay the onset of rapid aggregation. We also performed a structural analysis that reveals the power law dependence of aggregate fractal dimension (d_f) in both monoand bidisperse systems, with mean d_f consistent with diffusion-limited cluster aggregation (DLCA) aggregates. Our results also suggest that the d_f of aggregates is



insensitive to the shape anisotropy. We simulated molecular forces driving aggregation of polystyrene NPs of different sizes under high ionic strength conditions. These conditions represent salt concentration in ocean water and wastewater, where the DLVO theory does not apply. Our simulation results show that the aggregation tendency of the NPs increases with the ionic strength. The increase in the aggregation is caused by the depletion of clusters of ions from the NPs surface.

■ INTRODUCTION

Microplastics (MPs) and nanoplastics (NPs) have become a major environmental concern globally due to their extensive presence in aquatic systems. Once they enter water bodies, they undergo various transformations like degradation and aggregation, which affect their fate and transport, as well as removal from natural water bodies. 1-3 Thus, the aggregation of MPs and NPs in water significantly influences different natural and engineered processes, including environmental impact assessment and water/wastewater treatment. Therefore, it is crucial to gather and analyze quantitative data related to the dynamics and morphology of these aggregates in water.

In the existing literature, aggregation of MPs and NPs refers to the process by which primary particles assemble into large aggregates with a self-similar, fractal morphology.⁴⁻⁶ Aggregation kinetics display two limiting regimes: (i) diffusion-limited cluster aggregation (DLCA), in which particles associate upon collision, resulting in fast aggregation kinetics, and (ii) reactionlimited cluster aggregation (RLCA),8 in which only collisions that overcome an energy barrier result in irreversible association. Each regime has different rate-limiting physics, aggregation dynamics, and cluster-mass distributions. The fractal structure of aggregates has been frequently expressed in terms of a single exponent, the fractal dimension d_{θ} which reflects the scaling of mass of an aggregate (m) with its linear size, radius of gyration

 (R_g) , $m \propto R_g^{d_f.8}$ DLCA generates loose and ramified aggregates with a d_f of about 1.7, and RLCA produces more compact aggregates with a d_f of about 2.1, setting general limits on the d_f of $1.7 \ll d_f \ll 2.1$ primarily determined by 3D scattering (light, X-ray or neutron) techniques.^{9–11} Studies on the growth and morphology of aggregates have mainly focused on homogeneous and monodisperse particles despite reports of heteroaggregation of particles of different chemical compositions. 12-17 This is because the equations for aggregation are complex and difficult to solve rigorously, leading to the assumption of a monodisperse suspension, which has persisted over time. 18,19 Moreover, from an experimental perspective, these studies focus on either measuring aggregation kinetics using light scattering spectroscopy or visualizing aggregate morphology using traditional and cryogenic transmission electron microscopy (TEM) techniques. 20–25 The former can discern time-dependent aggregate ensemble properties based on the assumption of a

Received: April 1, 2024 Revised: June 9, 2024 Accepted: June 23, 2024 Published: July 5, 2024





Table 1. Representative Experimental Conditions for In Situ Microscopic Aggregation Experiments in This Study

MS suspension	Size (µm)	Concentration (mg/L)	IS (mM) ^a	
			RLCA	DLCA
Monodisperse	0.5	50 ± 8	50	500
Monodisperse	1.0	200 ± 25	50	500
Bidisperse	0.5 (50%) + 1.0 (50%) by vol.	125 ± 15	50	500

[&]quot;Please note that the IS used for RLCA and DLCA experiments are below and above the critical coagulation concentration (CCC) determined for each system in the pre-experiments, respectively.

homogeneous system. However, it poses challenges in interpreting results from polydisperse systems. The latter can allow for the visualization of aggregate structure and morphology down to the nanoscale. However, it cannot measure real-time aggregate growth. Therefore, the mechanisms for growth can only be inferred from the size and morphology of MPs/NPs ex situ. It is important to note that in situ TEM has shown promise as an effective approach to observing aggregate growth and structure at improved temporal and spatial resolutions. However, it has limitations for particles that exhibit low contrast in liquid samples, such as plastic nanoparticles. Nevertheless, these studies have significantly improved our understanding of the homoaggregation behavior of MPs and NPs in aquatic systems.

A comprehensive understanding of the aggregation behavior of MPs and NPs with varying sizes is still lacking, although this knowledge is crucial from both a practical and realistic perspective. For instance, it has been observed that in natural aquatic environments, MPs and NPs can range from 30 to 2000 nm in size. ^{2,3,29,30} This suggests that particles of different sizes are more likely to aggregate than particles of the same size. The information is crucial for predicting the behavior of MPs and NPs in the environment. Moreover, coagulation and flocculation processes are vital in water and wastewater treatment, but their models based on uniform particle size are only applicable in initial stages. The impact of primary particle distribution on coagulation and flocculation behavior is not well understood, making it important to study aggregating suspensions with different sizes to inform engineering aspects of these processes.

In the field of fractal physics, some attention has been given to the effects of polydispersity of primary particles on aggregate structure. 31-35 However, further understanding of its role in both aggregate growth kinetics and morphology is needed. Specifically, Eggersdorfer and Pratsinis³⁶ showed that colloidal suspensions exhibiting large polydispersity form open aggregates with $d_f = 1.5$, which is smaller than the typical d_f for DLCA, underlining the strong impact of particle size distribution on aggregate structure. Interestingly, by performing DLCA simulations with multiple primary particle sizes, Bushell and Amal³⁷ showed that the fractal structure and the form of the cutoff functions that describe the shape of aggregates are unaffected by the details of the primary particle size distribution, while the partial structure factor depends on the primary particle size distribution. Tence et al.³⁸ also showed that polydispersity does not affect the fractal dimension. The experimental result for the fractal dimension is consistent with the cluster-cluster model with linear trajectories. There is still debate over how the primary particle size distribution influences the formation of their aggregates, including both kinetics and structure. Furthermore, aggregates often exhibit complex morphologies, including anisotropy in shape. ^{6,39,40} These characteristics have implications on the physical and transport properties of the aggregates, such as mechanical strength, density, and fluid drag

characteristics.⁴¹ In addition to the fractal dimension, understanding the anisotropy of aggregates is critical to fully describing their morphology and mobility in water. Further investigation is needed to understand how anisotropy and other structural characteristics, such as d_{fi} are related.

In this work, we investigate how the bimodal primary particle size distribution affects the formation of aggregates by nano- and microparticles in both mono- and bidisperse systems. Polystyrene microplastic spheres are selected due to their widespread presence in the environment and their use as a model for MPs and NPs in laboratory work. For the microparticle system, we conducted customized in situ microscopic experiments focusing on the growth kinetics of colloidal aggregates while simultaneously tracking their morphological changes. The study involved analyzing the growth curve, cluster size distribution, fractal dimension, and anisotropy to examine the aggregate kinetics, structural evolution, and morphologies. This information is typically difficult to obtain through traditional bulk measurements, such as dynamic light scattering (DLS), especially when primary particle size varies. For the nanoparticle system, our focus is on investigating how NPs of two different sizes form aggregates under varying high salt conditions. This information is crucial in understanding the behavior of NPs aggregation in aquatic environments like ocean water and wastewater with high ionic strengths such as hypersaline hydrofracturing brines. 42-44 However, this area of research has been limited in the past because most studies have focused on NP aggregation under low salt concentrations (<1M) in a monodisperse system which can be qualitatively described by the classic Derjaguin - Landau - Vervey -Overbeek (DLVO) theory.² However, recent evidence shows that DLVO theory breaks down at high salt concentrations. In such conditions, hydration effects, steric interactions among ions, and ion-ion correlations cannot be ignored.⁴⁵ To gain a molecular-level perspective, we conducted molecular simulations of polystyrene NPs of two different sizes under various high ionic strength conditions. We have discussed the results on the radial distribution function and aggregate size distribution obtained from these simulations.

EXPERIMENTAL SECTION

Mono- and Bidisperse Microparticle Suspension. Approximately spherical Carboxylate-functionalized polystyrene microspheres (MS) (Polyscience, Inc.) of two sizes were used as the primary particles to prepare the mono- and bidisperse microparticle suspension. We chose polystyrene microplastic spheres because they are commonly found in the environment and are used as a model for microplastics and nanoparticles in laboratory research. Additionally, the carboxylate functional group provides enough surface charge to keep the MPs stable without ionic strength, while adjusting the ionic strength can easily control different aggregation regimes. The diameters of smaller and larger MS were measured to be 0.50 \pm 0.01 μm and 1.0 \pm 0.02 μm , respectively. Analytical-grade NaCl electrolyte solutions were used to create different ionic strength conditions for the aggregation experi-

ments. NaOH (1M) and HCl (1M) were used to adjust the pH in all experiments. The details of the mono- and bidisperse MS suspensions used in this study are provided in Table 1. The bidisperse MS system was made up of 50% (vol.) d_p = 0.50 $\mu \rm m$ and 50% (vol.) d_p = 1.0 $\mu \rm m$ MS. In order to determine the surface charge properties of MS under different experimental conditions, we used the Zetasizer Nano (Malvern Panalytical Ltd.) to measure the electrokinetic properties, including zeta potential and electrophoretic mobility of MS in water. Each experimental condition was measured in triplicate. The Supporting Information (SI) contains Figure S1, presenting all zeta potential and electrophoretic mobility measurements.

In Situ Microscopic Experiments. We conducted aggregation measurements using a custom-made liquid cell mounted on an inverted optical microscope (Eclipse Ti-E, Nikon Instruments Inc. USA). We used a 100× oil immersion magnification objective and an Andor iXon3 EMCCD camera that was controlled by NIS Elements software (Nikon Instruments Inc., USA). We have previously described more details of this experimental setup in our earlier work. 46 In brief, to prepare a suspension with MPs at the targeted concentration, we mixed particles in water, dispersed them using a sonicator, and adjusted the pH by titration with HCl. Next, we added NaCl to induce the aggregation process. To avoid insufficient mixing, we introduced NaCl to the suspension before injecting it into the cell. Finally, we delivered/ injected the mixed suspension to the cell, which was sealed and mounted onto the microscope stage. The injection procedure for suspension usually lasted for around 1 min. Therefore, the beginning of microscopy observations at t = 0 corresponded to approximately 1 min after the suspension was dispersed. Images with a resolution of 0.04 μm/pixel were captured every 10 s until the aggregates reached maturity. After each experiment, a larger final image, 3 × 3 times larger than the image with a normal field of view, was captured to collect extensive data on the size and shape of saturated aggregates in a steady state. This study investigated two different aggregation regimes, RLCA and DLCA, regulated by varying ionic strengths. The aggregation of MPs in water was carried out at room temperature and a pH of 6 in all cases. Mass concentrations of mono- and bidisperse microplastic (MP) suspensions were prepared at 50 ± 8 ppm, 200 ± 25 ppm, and 125 ± 15 ppm for $d_p = 0.50 \ \mu \text{m}$ (monodisperse), $d_p = 1.0 \ \mu \text{m}$ (monodisperse), and $d_v = 0.50$ and 1.0 μ m (bidisperse), respectively. Our preliminary results indicate that these concentrations result in comparable surface concentrations of MPs in each setting, with approximately 1×10^3 particles visible in the field of view. It is worth mentioning that these mass concentrations are higher than those observed in the environment. The justification for selecting these high concentrations is as follows: a recent study on the mass concentration of microplastics in wastewater treatment plants estimated the mass concentration of total MPs in the influent to be 26.23 μ g/L.⁴⁷ However, this low concentration is insufficient for studying the aggregation behavior of microplastics in a small-volume device such as a liquid cell, as there are not enough particles to form aggregates under a typical field of view. In the current practice, microplastics are included as part of total suspension solids (TSS), which are reported to range from 50 to 400 ppm in the influent.⁴⁸ An important study in the literature suggests that diffusion-limited cluster aggregation (DLCA), which is the focus of our study as well, follows a universal aggregation regime. 49 This suggests that it is independent of the specific chemical nature of the colloids. Therefore, the results we derived from biodisperse MPs can be applicable to describe the aggregation of MPs with other natural colloids that have comparable size and surface properties used in our study. This is likely to occur in reality. Details of these in situ microscopic experiments are provided in Table 1.

Image Analysis. The acquired images were processed using image processing algorithms in MATLAB. The following steps were taken: First, the background noise was subtracted from each image. Next, image segmentation was performed using Otsu's thresholding method to generate binary images. These images were then used for subsequent analysis of aggregate growth. To determine the characteristic length of aggregates, a customized autocorrelation function based on fast Fourier transforms was used. The error was estimated using the bootstrap resampling method. Processing of the large 3 × 3 image for aggregate

structural analysis was initiated by applying a global thresholding method to obtain binary images. Figure S4 shows the steps involved in the processing and analysis of a large image. All objects (including single particles and aggregates) were identified and characterized by MATLAB bwlabel function and regionprops function, respectively. The procedure used to identify particles and aggregates is described in the Supporting Information (SI) section S2. The acceptable criteria used in our study to identify single particles and aggregates are illustrated in Figure S5. More detailed information about the autocorrelation function and structural analysis of aggregates are presented in the following section. It is important to note that our image analysis focused on 2D slices in the plane parallel to the coverslip of the liquid cell. Therefore, our results only reflect the structure of the aggregates in two dimensions and do not account for the complete 3D structure of the aggregates.

Determination of Characteristic Length. A customized autocorrelation function via fast Fourier transforms using the Wiener-Khinchin theorem was used to determine the characteristic length of aggregates.

$$S(I) = |\mathcal{F}[I(x, y)]|^2 \tag{1}$$

$$G(a, b) = \mathcal{F}^{-1}[S(I)] \tag{2}$$

where I(x,y) is the source image with intensities at positions (x,y), S(I) is the power spectrum of the image, G(a,b) is the autocorrelation image with spatial coordinates (a,b), F and F^{-1} denote the Fourier transform and the inverse Fourier transform, respectively. In brief, the microscopy source images were used to generate a 2D spatial autocorrelation image, which was then used to plot a radially averaged distribution. It has been demonstrated that this distribution can be fitted by an exponential function (SI Equation S5) to determine the characteristic length, λ , which is directly proportional to the radius of each aggregate, r, estimated by measuring the aggregate area in real dimensions, $\sqrt{A_a}$. More details can be found in the Supporting Information (SI) section S1, Figure S3, and our previous work.

Determination of Structural Properties. Self-similar aggregates form via aggregation and exhibit a scale-invariant nature described by the fractal dimension (d_f) , following the relation 37,51

$$N = k(R_g/a)^{d_f} \tag{3}$$

where N is the number of monomers/primary particles in an aggregate, determined by counting the number of pixels within each identified cluster and converting to real dimensions, k is the fractal prefactor or structure factor, a is the monomer radius and $R_{\rm g}$ is the radius of gyration of the aggregate. The $R_{\rm g}$ was calculated as

$$R_g = \sqrt{\sum_{i=1}^{i=1} \left[(x_i - x_c)^2 + (y_i - y_c)^2 \right] / (n-1)}$$
 (4)

where x_c and y_c are the x-y coordinates of the centroid of each cluster, x_i and y_i are the x-y coordinates of the i^{th} pixel in an aggregate, and n is the number of pixels in each aggregate.

For a 2D aggregate, the anisotropy (A) is the ratio of the squares of its principal radii

$$A = \frac{{R_1}^2}{{R_2}^2} \tag{5}$$

where R_1 and R_2 represent the principal radii of an aggregate and $R_1 \ge R_2$. More details regarding three length-based parameters, such as characteristic length, radius of gyration, and aggregate size, can be found in section S3.

Molecular Simulation Methodology. We performed molecular simulations of spherical polystyrene nanoparticles of different sizes and at different ionic strengths to understand their aggregation behavior. We utilized coarse-grained (CG) Wet Martini force field (v2.2) to model polystyrene particles, water, Na^+ , and Cl^{-12} We considered spherical polystyrene particles of two sizes: small styrene (radius = 0.8 nm) and large styrene (radius = 1.6 nm) (Figure 7A). The spherical

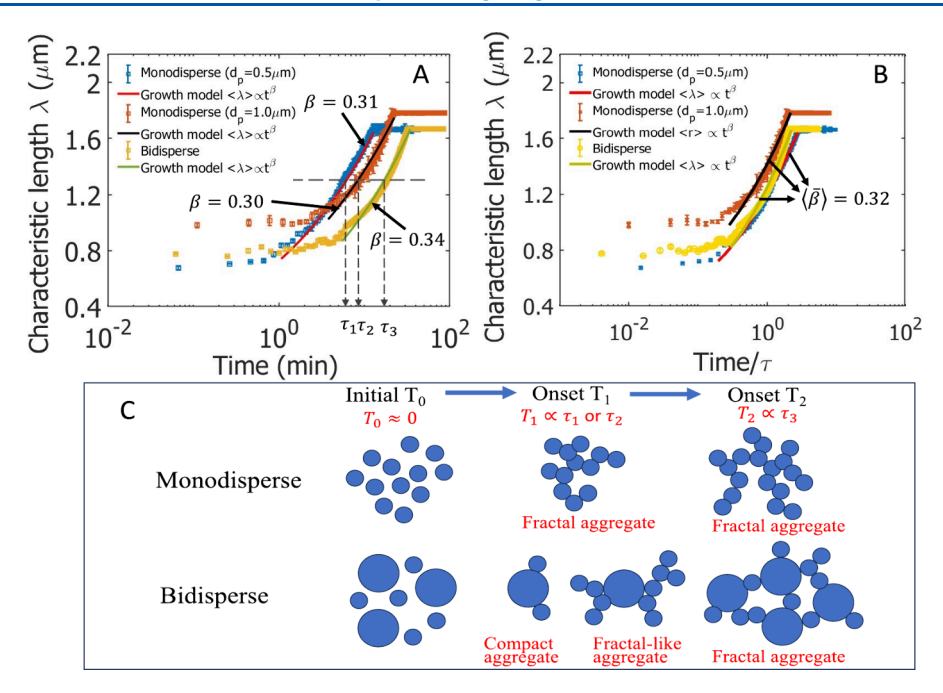


Figure 1. A: Characteristic length λ of clusters as a function of time in both mono- and bidisperse polystyrene microsphere (PS-MS) systems under fast aggregation (DLCA) conditions with IS = 0.500 M. d_p = 0.5 μm, 1.0 μm, and 0.5–1.0 μm are open squares, crosses, and spheres, respectively. A bootstrap method was used to evaluate the error in experimental data. Data in growth phases were fitted with a power law in the form of $\langle \lambda \rangle = Kt^{\beta}$, where β is the growth exponent. Reflecting points τ_1 , τ_2 , and τ_3 represent characteristic half aggregation times for experiments with d_p = 0.5 μm, 1.0 μm, and 0.5–1.0 μm, respectively. B: Data from (A) where time has been normalized, t/τ_i ; growth phase collapse or in parallel indicates the similarity of growth curves for both mono- and bidisperse PS-MS systems. C: A proposed mechanism of aggregation in a system with bimodal particle sizes.

nanoparticles were constructed by assembling polystyrene beads of diameter 0.41 nm on the surface of a sphere of radius r (= 0.8 nm for small and 1.6 nm for large nanoparticles). 52 The Lennard-Jones energy parameter, ε of the polystyrene beads was taken as 2.4 kJ/mol. ⁵² We performed molecular dynamics simulations of 82 small nanoparticles; 20 large nanoparticles; and a mixture of 41 small and 10 large nanoparticles in three different NaCl salt molarities (0.5, 1, 2 M). This range covers a wide variety of ionic strengths found in typical seawater and wastewater with high salt concentrations. 53,54 The simulation box was considered periodic in the three directions with the average size of $25 \times 25 \times 25$ nm³. Styrene particles interact with other styrene particles as well as water and ions via Lennard-Jones interactions. We used a spherical cutoff of 1.4 nm for the Lennard-Jones interactions. Coulombic interactions were modeled using Reaction-Field-zero (RF-zero) with a spherical cutoff of 1.4 nm, and the relative dielectric constant was set at 2.5. Both Lennard-Jones and Coulombic interactions were smoothly shifted to zero beyond the cutoff. To regulate the temperature and pressure, we utilized the Bussi et al. velocity-rescaling thermostat and the Parrinello-Rahman barostat with isotropic coupling and a coupling time constant of 12 ps.³ The isothermal compressibility and reference pressure were set to 3×10^{-4} bar⁻¹ and 1.0 bar, respectively. All simulations were performed using the GROMACS/5.1.2 molecular simulation package.⁴ The results were postprocessed using Python scripts.

The initial configuration of the system was energy minimized using the steepest descent algorithm with a maximum force tolerance of $1000.0 \text{ kJ mol}^{-1} \text{ nm}^{-1}$, followed by a 100 ns canonical ensemble (constant number of particles N, volume V, and temperature T) simulation with a 10 fs time step for pre-equilibration. Three independent isothermal—isobaric (constant N, pressure P, T) ensemble simulations were then performed for each condition for 800 ns with a 10 fs time step. Simulation data was collected for the last 300 ns. This duration of the production runs was adequate to ensure a robust statistical analysis of the molecular configurations of the systems.

We determined the size distribution of the nanoparticle aggregates that formed in different conditions in the simulations. Two polystyrene particles were assigned to the same aggregate if the distance between the center of mass of any of the constituent polystyrene beads in the two nanoparticles was less than 3 Å. We also calculated their radial distribution function, g(r). The g(r) is a measure of the probability of finding a particle at a specific distance from a reference particle. The g(r) is useful for studying the structure of particle aggregates.

■ RESULTS AND DISCUSSION

In Situ Microscopy of Diffusion- and Reaction-Limited Cluster Aggregation. Aggregate Growth Curve. The characteristic length (λ), determined from the autocorrelation function, was utilized to study the aggregation kinetics of micron-sized particles in both mono- and bidisperse systems. Figures 1 and S2 depict the growth of the average cluster/ aggregate size (λ) over time under typical DLCA and RLCA aggregation conditions, respectively. Throughout our experiments, we notice that regardless of the molarity, there is a noticeable delay in the aggregation process before it rapidly accelerates (early stage). During this initial stage, the kinetics of our experiments share similarities with the RLCA process. In the following growth period (middle stage), the size of the aggregates increases nearly linearly with time on a semilog plot, indicating a power-law growth behavior. In the late stage, the characteristic length (λ) reaches a saturated value due to a finite supply of particles, consistent with prior research. ^{49,50} In both mono- and bidisperse systems, it is observed that there is a transition from slow to fast aggregation. This can be explained by the increased contact points between larger clusters, which leads to a greater probability of cluster-cluster sticking as the clusters grow. Despite the small probability of irreversible reactions during the first contact, the phenomenon persists. Previous studies have shown that the rate at which clusters grow can be linked to the diffusion coefficient of individual clusters when the growth process is dominated by cluster diffusion. 55 Specifically, if the particles are assumed to be 2D clusters diffusing by

Brownian motion, a scaling analysis of the Stokes-Einstein diffusivity equation yields a Smoluchowski growth exponent (β) of 1/3 by $\beta = 1/2(\sigma + 1)$, where σ is the 2D diffusion scaling exponent, which equals to 1/2. 55,56 These findings are consistent with the mean growth exponent of 0.32 observed in both monoand bidisperse DLCA aggregation experiments, despite a slightly higher growth exponent in the bidisperse system, as shown in Figure 1. The results also indicate that the bimodal particle size distribution shifts the growth curves, thus delaying the onset of rapid aggregation in the bidisperse systems (Figure 1A). However, normalizing the aggregation time (t) using a characteristic aggregation time (t_{50}) shows that the growth curves either collapse onto each other or have the same slope (Figure 1B), indicating similar aggregate growth mechanisms for both mono- and bidisperse systems. This evidence suggests that the primary particle size distribution has little effect on the kinetics of the scaling behavior of aggregate growth but significantly delays the onset of rapid aggregation. We propose the following mechanism for how bimodal particle size affects fast aggregation onset in bidisperse systems (Figure 1C): In the initial stage $(T_0 \approx 0)$, particles in both mono- and bidisperse systems undergo Brownian motion. Due to the size-dependent diffusion coefficients, small particles diffuse faster than large particles. When particles come close to each other, they collide and form aggregates. In the early T_1 stage $(T_1 \propto \tau_1 \text{ or } \tau_2)$, which corresponds to the onset of fast aggregation for monodisperse particles, aggregates with fractal structure begin forming in the system. However, in the bidisperse system, simultaneously formed aggregates exhibit a wide range of morphologies, including relatively small but compact aggregates formed by large particles scavenging small particles and relatively large but open aggregates composed of a large number of small particles and a small number of large particles and with a structure close to fractal nature (fractal-like). This broad variation in aggregate structures is not so prominent in the monodisperse system, resulting in the aggregates in the bidisperse system at this stage not exhibiting a well-characterized fractal structure as an ensemble. These aggregates with a broad range of morphologies collide further and form larger aggregates. At the later stage T_2 $(T_2 \propto \tau_3)$, which corresponds to the onset of fast aggregation for bidisperse particles, large aggregates with fractal structures are finally formed. In other words, in the bidisperse system, it takes a longer time or requires more primary particles to form aggregates with DLCA structure. While the proposed mechanism discussed above matches our experimental findings, we acknowledge that more work needs to be done to firmly establish the aggregation mechanism in bidisperse systems. Moreover, in this study, aggregation processes for RLCA and DLCA were initiated by adding IS at 50 mM and 500 mM, respectively. It is important to note that these values are below and above the Critical Coagulation Concentration (CCC) determined for each system in the pre-experiments, respectively. In the DLCA regime, we observed that the aggregate growth follows a power-law behavior, with a growth exponent of 0.32, which aligns well with the classic DLCA kinetics in the literature. \$7,58 On the other hand, in the RLCA regime, understanding aggregate growth kinetics is challenging. At low IS in the RLCA regime, the average aggregate size grows exponentially with time,⁵⁵ whereas at relatively high IS in the RLCA regime (also referred to as the intermediate regime between RLCA and DLCA in the literature), the aggregate grows according to a power law with an exponent varying continuously within the range of IS.⁵⁹ Due to the limited IS

scenarios used in this study, we cannot confidently fit the growth curve to quantitatively test these relations. Further investigations are needed to fully understand the RLCA kinetics.

Aggregate Structure and Morphology. Aggregate Anisotropy. The time evolution of the aggregate anisotropy for typical RLCA and DLCA aggregation experiments in both mono- and bidisperse systems is presented in Figure 2A–B. The results

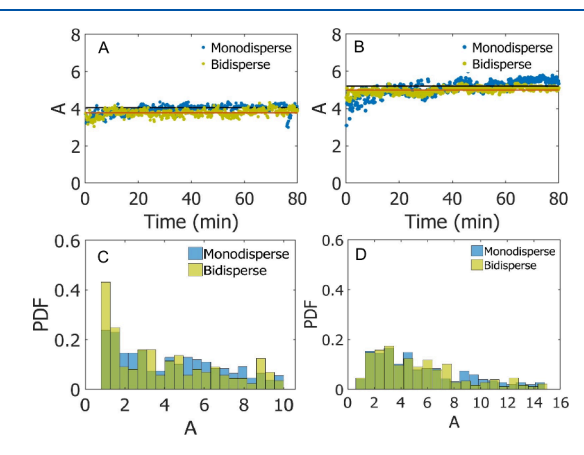


Figure 2. Evolution of anisotropy (A) as a function of time in both monodisperse ($d_p=1.0~\mu\mathrm{m}$) and bidisperse ($d_p=0.5~\mathrm{and}~1.0~\mu\mathrm{m}$) systems under RLCA (A) and DLCA (B) regimes. Each point displays the average A of all aggregates in an image captured at time t. C and D represent the probability density function (PDF) of the anisotropy of aggregates in mono- and bidisperse systems in the late stage of aggregation, under RLCA and DLCA regimes, respectively. To determine the PDF of A, for the RLCA monodisperse system, approximately 686 aggregates were analyzed, while around 703 aggregates were analyzed for the bidisperse system. Similarly, for the DLCA monodisperse system, nearly 514 aggregates were analyzed, while roughly 504 aggregates were analyzed for the bidisperse system.

indicate that there is no systematic change in the anisotropy over time as the aggregation proceeds, despite the different mechanisms of aggregation. Therefore, it is justifiable to average the measured anisotropy during the entire aggregate growth under given experimental conditions to evaluate the effects of aggregation mechanisms on the aggregate anisotropy. The results indicate that the averaged anisotropy is influenced by the mechanisms that control aggregation. The averaged anisotropy determined in the DLCA regime is slightly larger than that in the RLCA regime (Figure 2A-B). The results also indicate that the anisotropy values of aggregates formed in the bidisperse system are slightly smaller than those formed in the monodisperse systems, particularly in DLCA aggregation experiments. However, this difference is not significant compared to the measured error. The results of the probability density function (PDF) of the anisotropy (Figure 2C-D) measured at the late stage of aggregation indicate that the anisotropy of aggregates varies widely in both mono- and bidisperse systems.

Aggregate Fractal Dimension. Figure 3 shows typical double-logarithmic plots of $N=k(R_g/a)^{d_f}$ (eq 3) for aggregates investigated in this work. Aggregates exhibit scale invariance for the large aggregates investigated in this study. However, small aggregates appear to differ from the asymptotic scale invariance of the larger ones with slopes larger than 2. This suggests that small aggregates are dense and compact, and eq 3 cannot be used to estimate the true d_f of these aggregates. Instead, we calculated a perimeter-based fractal dimension (d_{pf}) by $A \propto P^{2/d_{pf}}$, 60 where A is the area of aggregate and P is the perimeter of aggregate. The

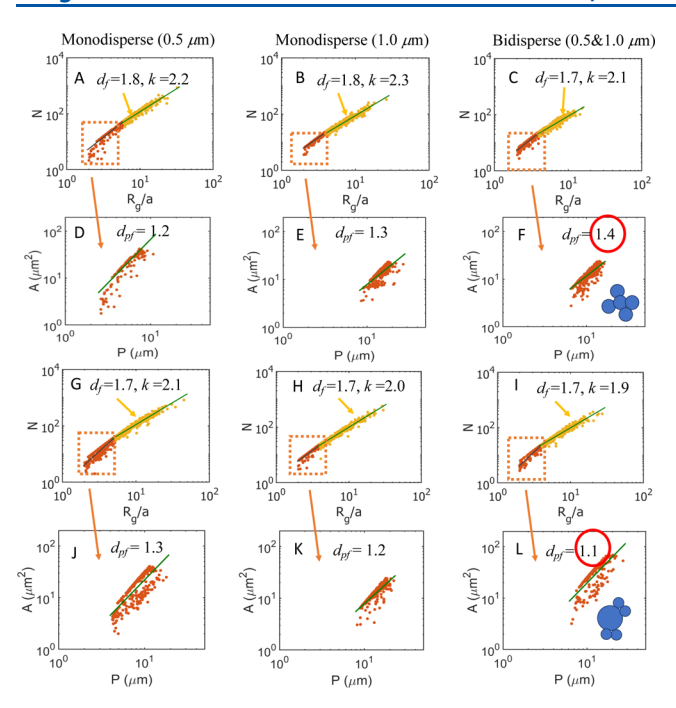


Figure 3. Structural analysis of aggregates in monodisperse and bidisperse systems. Log-log plots of N as a function of R_{ν}/a for the aggregates formed under RLCA (A-C) and DLCA (G-I) regimes, respectively. The results show that large aggregates can be best fitted by the fractal scaling described by eq 3. However, the small aggregates cannot be described by eq 3 because the slopes on the log-log plots are larger than 2. For these small compact aggregates, we estimate a perimeter-based fractal dimension $(d_{\it pf})$ by $A \propto P^{2/d_{\it pf}}$, 60 where A is the area of the aggregate and P is the perimeter of the aggregate (D-F and **J–L**). The real fractal dimension (d_f) in 3D can be determined by d_f = $-1.5d_{pf}$ + 4.4.⁶⁰ For the RLCA regime, the d_f values of small aggregates in monodisperse (0.5 μ m), monodisperse (1.0 μ m), and bidisperse (0.5 and 1.0 μ m) are 2.6, 2.4, and 2.3, respectively. For the DLCA regime, the d_f values of small aggregates in monodisperse (0.5 μ m), monodisperse (1.0 μ m), and bidisperse (0.5 and 1.0 μ m) are 2.4, 2.6, and 2.7, respectively. Tables S2-S5 show the goodness of these fittings. It is worth noting that the individual primary particles are excluded from this analysis.

real d_f (3D) of these compact aggregates can be further determined through the following correlation: $d_f = -1.5d_{pf}$ + 4.4. Thus, for the RLCA regime, the d_f of small aggregates in monodisperse (0.5 μ m), monodisperse (1.0 μ m), and bidisperse (0.5 and 1.0 μ m) are 2.6, 2.4, and 2.3, respectively. For the DLCA regime, the d_f of small aggregates in monodisperse (0.5) μ m), monodisperse (1.0 μ m), and bidisperse (0.5 and 1.0 μ m) are 2.4, 2.6, and 2.7, respectively. Please note that it is widely accepted that if the fractal dimension (d_f) determined from a 2D projection is less than 2, it can represent the d_f determined from a 3D system. 11 We have chosen not to use d_{pf} to quantify the large aggregates because the correlation between d_{pf} and d_f for fractal structure is unknown. This prevents us from comparing our results with the d_f in the existing literature. After analyzing the data, it appears that the aggregates formed under the RLCA regime are more densely packed than those formed under the DLCA regime in monodisperse systems. The fractal dimensions of these aggregates are consistent with the theoretical predictions and experimental evidence available in the literature for two-dimensional RLCA and DLCA. 38,49 However, this trend is not observed in the bidisperse system. In particular, large aggregates formed under RLCA and DLCA regimes exhibit

similar fractal structures with $d_f = 1.7$. It was also observed that small aggregates formed under the RLCA and DLCA regimes exhibit significantly different structures and morphologies. The d_f of small aggregates under the RLCA regime is 2.3 ($d_{pf} = 1.4$), whereas the d_f of small aggregates under the DLCA regime is as high as 2.7 ($d_{nf} = 1.1$). After closely examining these aggregates, it was found that the small aggregates under the RLCA regime are compact and mainly composed of small particles. This is due to the high energy barrier preventing large particles from interacting with small ones. On the other hand, the small aggregates under the DLCA regime are more compact and mainly comprise large particles that have gathered small particles on the edge. This is because the significantly reduced energy barrier in DLCA allows large particles to collide with small ones. This explains why the small aggregates formed in a bidisperse system have a larger fractal dimension in the DLCA regime than that obtained in the RLCA regime. (Figure 3F and 3L). In addition, based on the aggregation experiments studied in this work, it appears reasonable to divide the anisotropy results into two groups based on the fractal dimension. It is observed that for aggregates there is a consistent decrease in anisotropy as the fractal dimension increases (Figure 4C). To further investigate

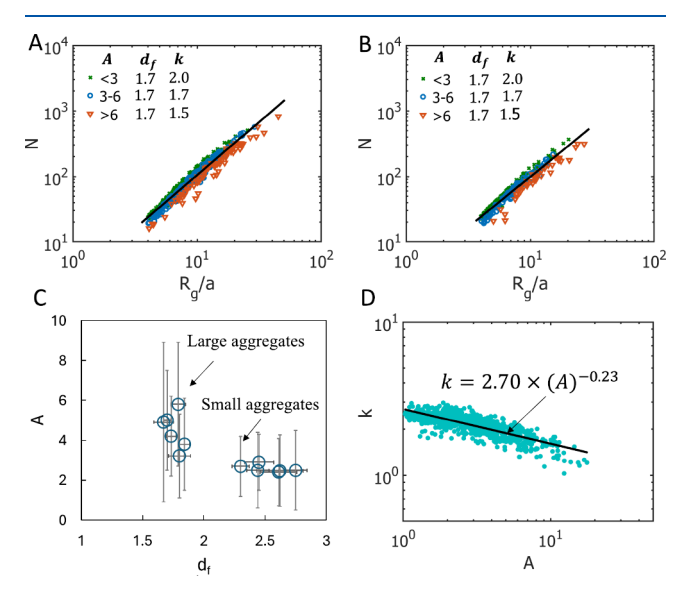


Figure 4. Number of primary particles, N, versus radius of gyration, R_g , normalized by primary particle size a, for DLCA large aggregates in (A) monodisperse and (B) bidisperse systems. The aggregates are classified by the bins of anisotropy (demonstrated by colors). C: The averaged anisotropy versus the fractal dimension determined from the aggregates investigated in this study. The error bar represents the standard deviations of d_f and A. D: The prefactor k versus k for individual DLCA aggregates. The solid line represents the best fit line $k = 2.70 \times (A)^{-0.23}$ when $k_f = 1.7$.

how the anisotropy of large aggregates affects their fractal dimension, we categorized the aggregates based on their anisotropy value and calculated the fractal dimension for each category using the scaling relationship described in eq 3. We found that the mean fractal dimensions of aggregates in each anisotropy category are very similar in both monoand bidisperse systems. Furthermore, it was observed that the aggregates with higher anisotropy values tended to be below the best-fit line for all the aggregates (Figure 4A–B). This results in smaller values for the prefactor k, indicating that anisotropy does indeed affect the prefactor k. In other words, for an aggregate

with fixed d_{t} if anisotropy increases, k decreases and vice versa, suggesting that local structure represented by k has an effect on large-scale structure represented by anisotropy and vice versa. It is worth noting that these findings are in agreement with the importance of the prefactor k as a descriptor of aggregate morphology, proposed by Heinson et al.⁵¹ who argued that shape anisotropy affects the prefactor, rendering k as a shape indicator. Moreover, we remark that anisotropies extend over a large range of values, even for the same $(d_{\theta} k)$. Our results also suggest an anticorrelation between A and k quantitatively. This is demonstrated by the best-fit equation as $k = 2.70(A)^{-0.23}$. The average anisotropy of DLCA aggregates was measured to be $\langle A \rangle$ = 4.0, the equation above or equivalently the solid line in Figure 4D yields $\langle k \rangle = 1.96$, in good agreement with previous results. ^{51,61} We further conducted the uncertainty analysis of the estimated fractal dimensions, and the results show that the 95% confidence intervals (CI) of d_f for aggregates with A > 6 are slightly larger than those of aggregates in the other categories. This is likely due to the smaller size of aggregates in this category for a typical DLCA experiment (Figure 5A). To confirm this, we

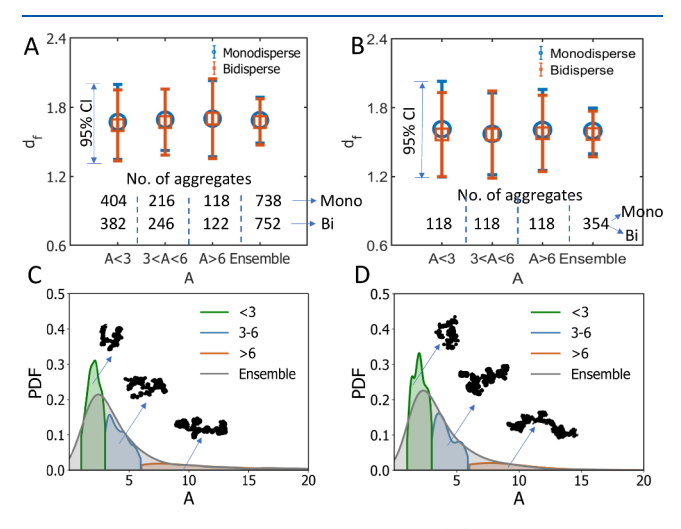


Figure 5. A: The estimated fractal dimension (d_f) and 95% confidence intervals (CI) of large DLCA aggregates in monodisperse and bidisperse systems. The number of aggregates in each anisotropy (A) category represents the number of aggregates collected in each system. B: The estimated d_f and 95% CI of large DLCA aggregates in monodisperse and bidisperse systems. In this case, the number of aggregates is fixed at 118 to eliminate the sample size effects on the 95% CI of d_f C-D: PDF of the A of large aggregates for each category in a typical monodisperse (C) and bidisperse (D) DLCA experiment.

further resampled the aggregates in each anisotropy category with a fixed sample size (118 aggregates). The results show that the 95% CI of d_f is very close, indicating that the d_f of aggregates from each anisotropy category has the same population characteristics (Figure 5B). It is worth noting that the d_f of the aggregate from the ensemble has a narrower confidence interval than that from different anisotropy, mainly due to the larger sample size. Furthermore, the PDFs of aggregate shape anisotropy in both monodisperse and bidisperse systems are similar, with the majority of aggregates being isotropic or close to isotropic in shape (Figure 5C–D).

Aggregate Size Distributions. As the growth kinetics are reflected in the aggregate size distribution, we have conducted measurements of the size distribution of aggregates in both mono- and bidisperse systems, along with its time dependence. To facilitate direct comparison with theoretical predictions

(Figure 6), the cumulative cluster size distribution in both mono- and bidisperse systems has been normalized by its mean value as $r/\langle r \rangle$. According to Smoluchowski kinetics, a classical model that describes the time evolution of an ensemble of particles as they aggregate, a characteristic analytical solution for particle size distribution in the long-time limit can be written as 55,56

$$F(\varphi) = \frac{2W}{\Gamma(\sigma+1)} (W\varphi)^{2a+1} e^{-(W\varphi)^2}$$
(6)

$$W = (\sigma + 1) \frac{\Gamma(\sigma + 3/2)}{\Gamma(\sigma + 2)} \tag{7}$$

where $F(\varphi)$ is the analytical particle size distribution scaled to the average particle size, $\varphi = r/\langle r \rangle$, Γ is the standard Gamma function, and σ is the scaling exponent for particle/cluster diffusion. As we discussed in the growth curve section, we assumed $\sigma = 1/2$ for 2D Brownian aggregates. Figure 6A displays that the size distribution of the experimental aggregates in the monodisperse system is in good agreement with the predictions made by the Smoluchowski model. However, in the bidisperse system, the aggregate size distribution is not precisely described by the Smoluchowski model. Specifically, the Smoluchowski model underestimates the number of aggregates that are smaller than the average size and overestimates the number of aggregates that are larger than the average size. Despite these differences, the Smoluchowski model still provides a relatively good approximation of the true aggregate size distribution in the bidisperse system. We have found that these discrepancies are due to the time-dependent Smoluchowski (collision) kernel. The original Smoluchowski kernel relies on the spatial correlations between different-sized aggregates and is understood to be independent of time. However, upon examining the aggregates of different sizes during various stages of aggregation, we observe that these distributions are time-dependent (Figure **6B–D**). The kinetic results have shown that primary particles that are monodisperse tend to form aggregates with an asymptotic fractal structure earlier than those that are bidisperse. This leads to a reduction in the time dependence of the Smoluchowski kernel in the monodisperse system, resulting in good agreement with the model prediction. However, in the bidisperse system, it takes longer to form aggregates with an asymptotic fractal structure. Thus, the time effects on the kernel become non-negligible, resulting in a noticeable discrepancy between experimental observations and model predictions. These results suggest that future studies are required to consider the time-dependent spatial correlations between aggregates of different sizes when applying the true time-dependent collision kernel in the Smoluchowski model to predict the size distribution of aggregates in a bidisperse system.

Simulation Results. We have studied the aggregation behavior of polystyrene nanoparticles of two different diameters, 1.6 nm (small) and 3.2 nm (large) as well as their bidisperse system using molecular simulations. In these simulations, we varied the ionic strength of NaCl to investigate its effect on the aggregation tendency of the nanoparticles. Figure 8 shows the size distribution aggregates for the small and the large nanoparticles in different NaCl salt concentrations. Figure 7C shows snapshots of the equilibrium configurations of the small, large and bidisperse systems in different salt concentrations. It is observed that the aggregation increases with the salt concentration for both the small and the large nanoparticles. To understand the effect of salt concentration, we compared the

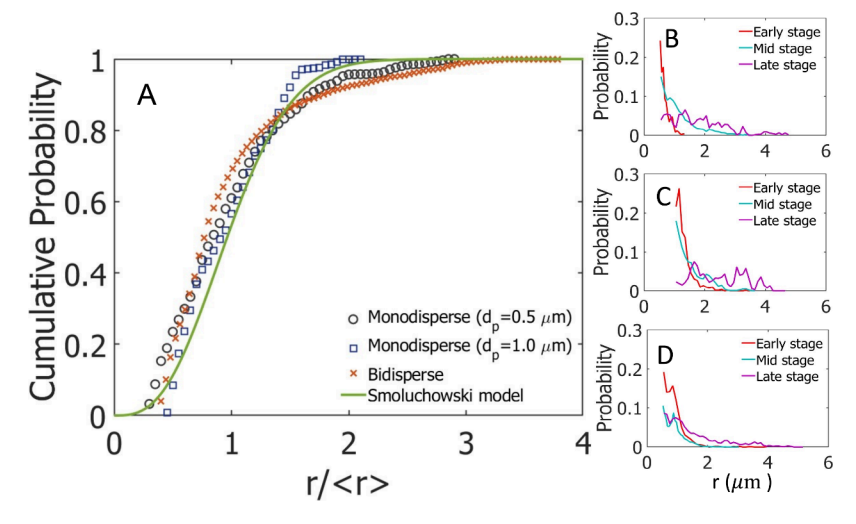


Figure 6. A: The cumulative probability distribution of DLCA aggregates during the aggregation process in mono- and bidisperse PS-MS systems and comparison with theoretical Smoluchowski distribution. To facilitate comparison, the aggregate size (r) was normalized by its respective mean size. The aggregate size distribution at different growth stages was observed in different experiments: ($\bf B$) monodisperse $d_p=0.5~\mu m$, ($\bf C$) monodisperse $d_p=1.0~\mu m$, and ($\bf D$) bidisperse ($d_p=0.5~and~1~\mu m$). It is worth noting that the aggregate size (r) represents the individual aggregate size at different stages, as determined by $\sqrt{A_a}$, where A_a is the aggregate area measured in real dimensions.

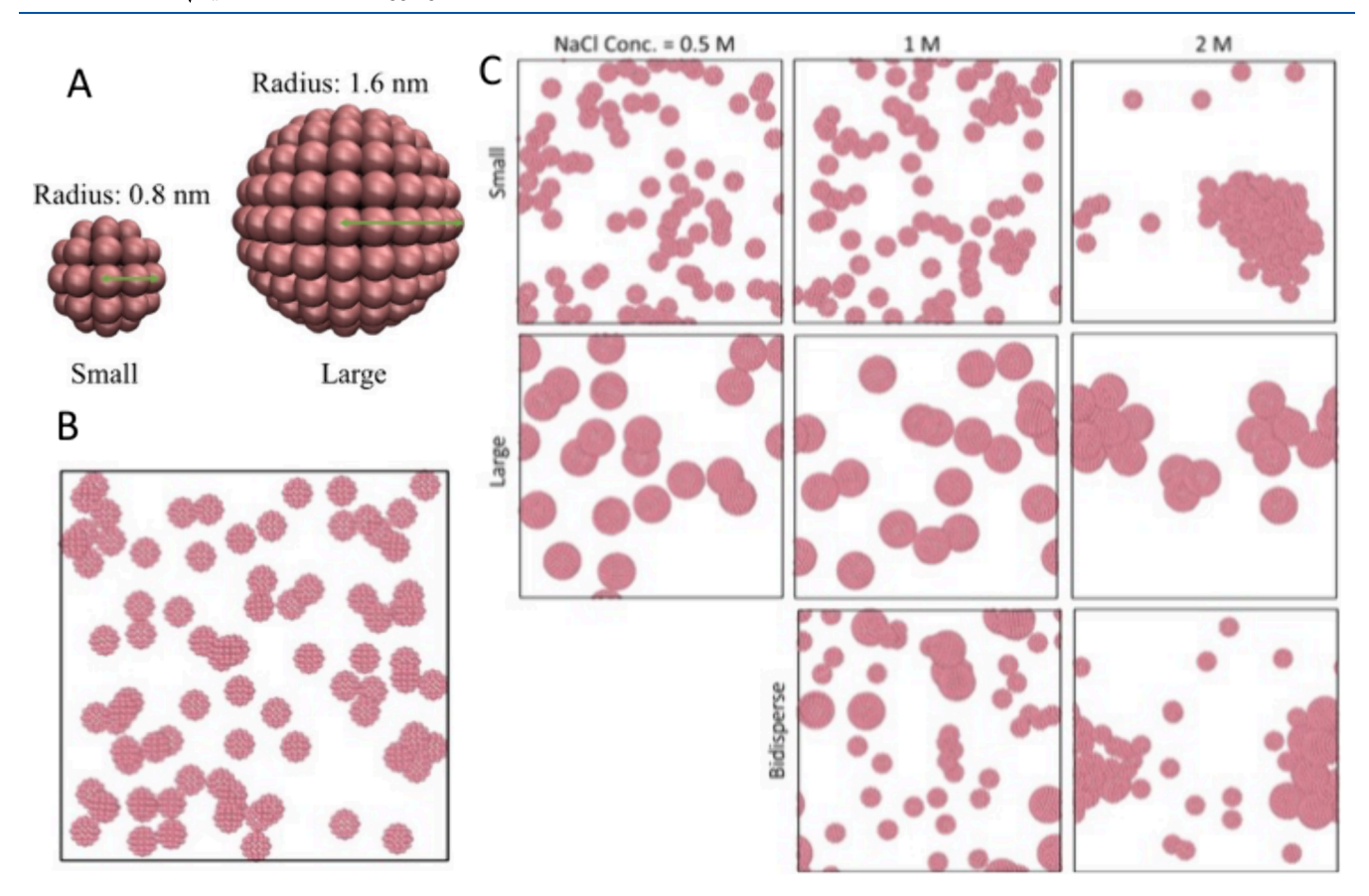


Figure 7. A: Snapshots of small (radius 0.8 nm) and large (radius 1.6 nm) spherical polystyrene nanoparticles. B: A snapshot of the initial configuration of small polystyrene nanoparticles in the simulation system. Water molecules and Na^+ and Cl^- ions are not shown for clarity. C: Equilibrium snapshots of the polystyrene aggregates as a function of NaCl salt concentration for the small particles (top row), the large particles (middle row), and the bidisperse system (bottom row).

radial distribution function, g(r), between the center of mass of the nanoparticles (COM) with Na⁺, Cl⁻ and with water (Figure 9). It is observed that both Na⁺ and Cl⁻ ions are excluded from the first hydration shell surrounding the nanoparticles. This occurs because these ions are strongly solvated in water. The

solvation shell gets disrupted if the ions enter the first hydration shell. Monovalent ions are known to form clusters as the ionic concentration increases. These clusters of ions have much larger excluded volume as single ions. Therefore, as the ionic concentration increases, the depletion of these ionic clusters

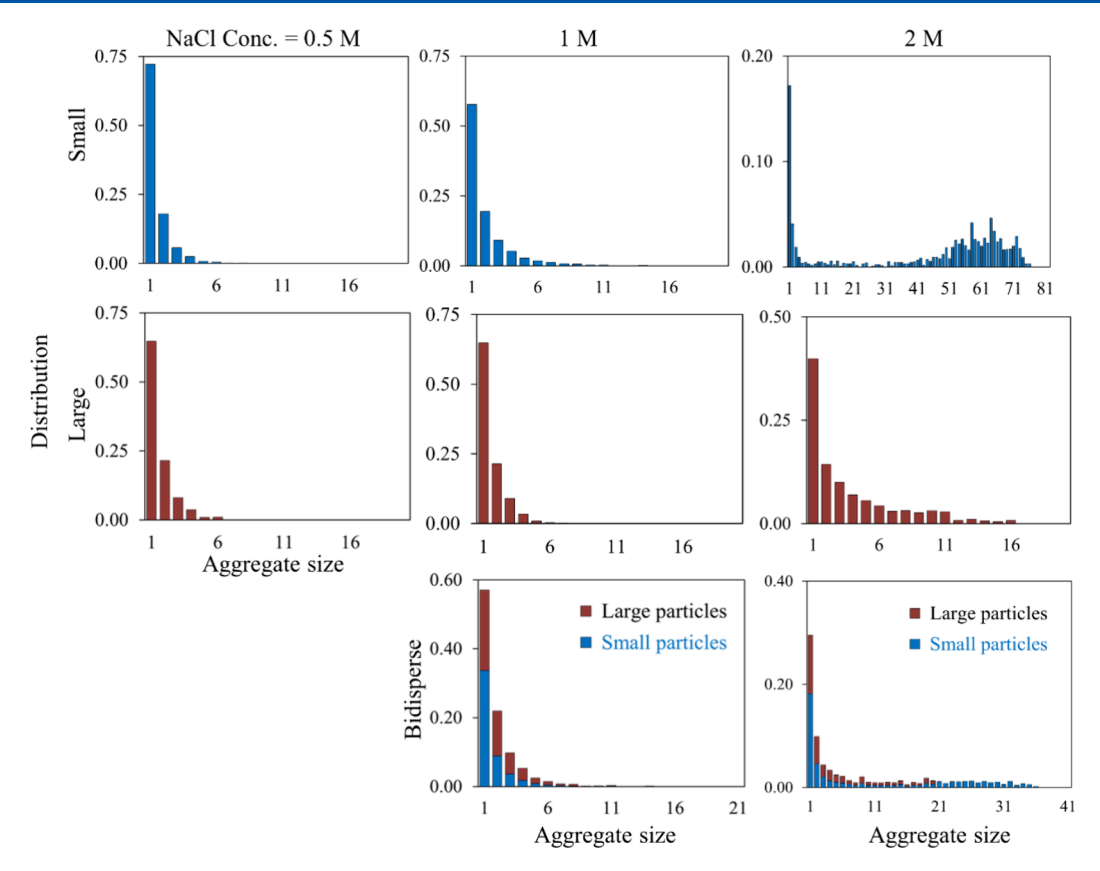


Figure 8. Polystyrene aggregate size distribution as a function of NaCl concentration for the small particles (top row), the large particles (middle row), and the bidisperse system (bottom row). The aggregation tendency increases with the salt concentration.

from the nanoparticle surface enhances their aggregation. ⁶² The exclusion of ions from the solvation shell of the nanoparticles is also observed in the bidisperse system shown in Figure 9. It should be noted that the g(r) are normalized by the bulk density of particles. At any distance r, the number of particles is given by $\rho g(r)$, where ρ is the bulk density. This implies that though the g(r) of Na-COM for the 0.5 and 1.0 M concentrations are indistinguishable from each other, twice the number of Na⁺ ions are excluded from the nanoparticles' surface at 1 M concentration as compared to 0.5 M concentration. Figure 10 shows the g(r) between Na⁺ and Cl⁻ ions at different concentrations and for the studied systems. A large peak is observed at a distance of 4.75 Å, which suggests that at these concentrations, the Na⁺ and Cl⁻ ions exist as clusters.

CONCLUSIONS

This study aims to examine the formation of micro- and nanosized plastic particle aggregates in aqueous systems with one or two sizes of primary particles. Our experimental results generally show that as the ionic strength increases in both monoand bidisperse systems, there is a transition from RLCA to DLCA-like phenomena in the kinetics of aggregation. The scaling behavior of aggregate growth is not significantly affected by the primary particle size distribution, but it does delay the onset of rapid aggregation. The structural analysis shows that the structure of aggregates formed in both mono- and bidisperse systems follows a power law dependence with mean d_{fp} consistent with DLCA aggregate fractal dimensions. This work also involved using molecular simulation to study the interaction between nanoparticles (NPs) of different sizes in aqueous solutions containing high concentrations of monovalent salt. We

observe that as the ionic strength of the solution increases, the aggregation tendency of the polystyrene nanoparticles is heightened. This strong attraction is not the typical charge-like electrostatic attraction but rather is due to the depletion effect of clusters of ions. The results of this study indicate that particle size distribution primarily influences the kinetics of aggregation by delaying the start of rapid aggregation. This has potential implications for water and wastewater treatment, suggesting that the presence of particles of different sizes may necessitate adjustments to retention time in order to achieve effective coagulation and flocculation.

Lastly, it is essential to acknowledge the limitations of our current study as follows: 1) the *in situ* microscopic experimental approach allowed us to observe aggregate growth and characterize its structure directly, but it presented technical challenges in dealing with a wide range of primary particle sizes. Specifically, it is difficult to capture two particles of significantly different sizes on the same focal plane when they are diffusing in a liquid cell due to the effects of sedimentation. To mitigate this issue, we opted to use two particles with sizes that are not significantly different to minimize the effects of sedimentation on the observation of aggregation kinetics. It is important to note that by simulation, Goudeli et al.³³ reported that increasing the width or polydispersity of the primary size distribution initially improves the collision frequency, but delays the attainment of the asymptotic fractal-like structure and selfpreserving size distribution without altering them. These findings align with our study and indicate that the results from our study are applicable to systems with a broader particle size distribution. Nevertheless, further research is encouraged to validate and extend these findings to a broader range of micron-

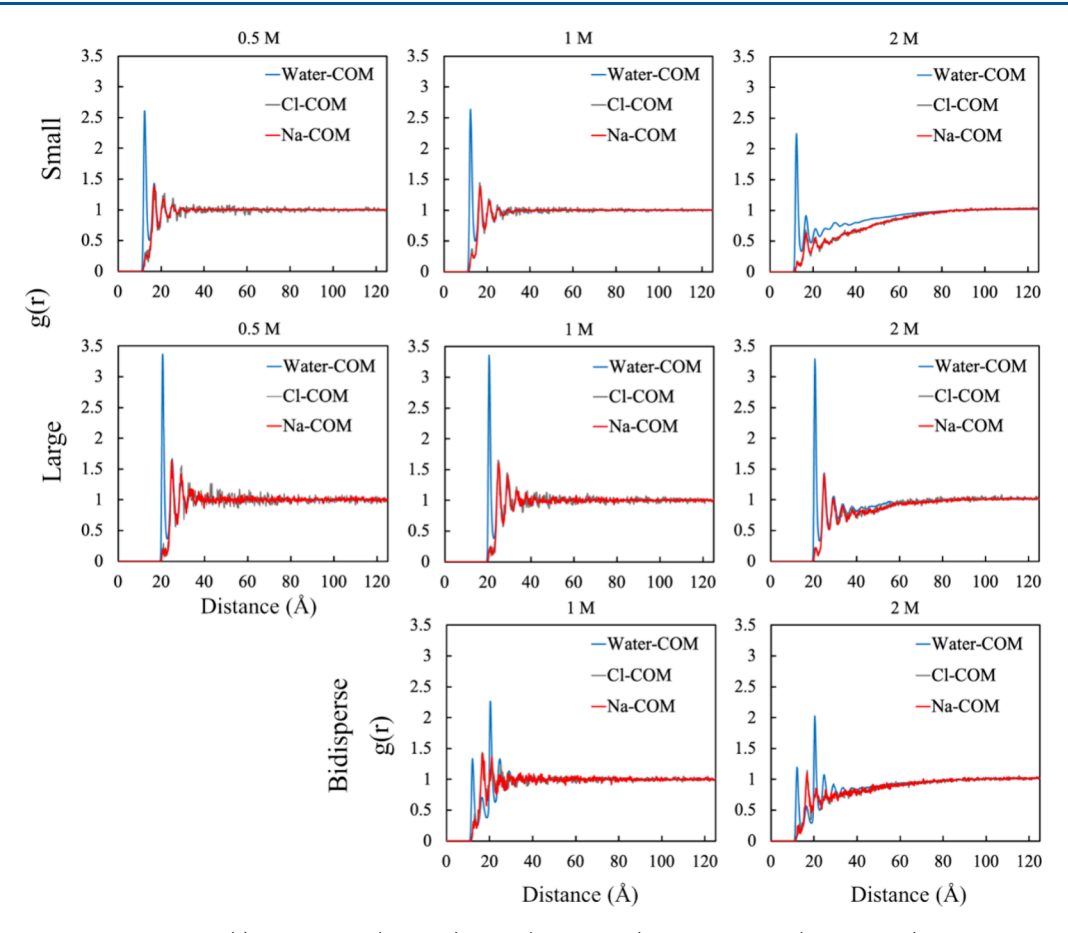


Figure 9. Radial distribution function, g(r), of the small (top row), large (middle row), and bidisperse (bottom row) polystyrene particles' center of mass (COM) with water and Na⁺ and Cl⁻ ions. In each case, Na⁺ and Cl⁻ ions are excluded from the first solvation shell around the nanoparticles. This explains the increased aggregation tendency of the nanoparticles with the salt concentration.

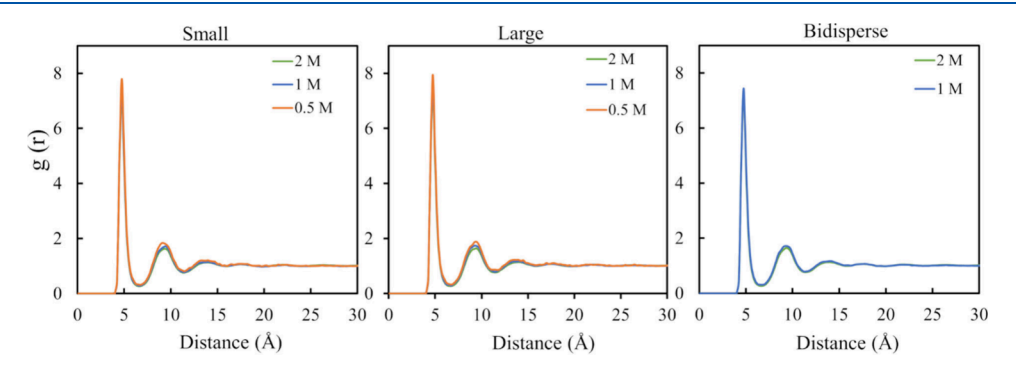


Figure 10. Radial distribution function, g(r), between Na⁺ and Cl⁻ ions at different concentrations and for the small nanoparticle, large nanoparticle, and bidisperse systems. In all cases, a large peak at a distance of 4.75 Å is observed, which reveals that the Na⁺ and Cl⁻ ions exist as clusters at these concentrations.

and nanosized MP particles; 2) The study aims to determine how the bimodal particle size distribution affects the formation of their aggregates. The aggregation of microplastics and nanoparticles in the real world is a complex process. This study focused on using model polystyrene microplastic spheres to exclusively investigate the effects of particle size distribution. However, further research using naturally aged microplastics and different conditions is encouraged to validate, modify, and improve the findings. and 3) we also must mention that we realized that our simulation system was relatively small, which prevented us from obtaining a statistically robust description of the structural features of the nanoaggregates. Thus, we did not

incorporate a structural analysis of the nano aggregates in our manuscript. Future studies involving a large simulation system should reveal the structure of nano aggregates formed by bi- or poly disperse primary particles.

ASSOCIATED CONTENT

Supporting Information

The Supporting Information is available free of charge at https://pubs.acs.org/doi/10.1021/acs.langmuir.4c01216.

Autocorrelation function; characterization of image objects as small and large aggregate clusters; aggregate size, radius of gyration, and characteristic length; and the

statistical summaries of fitting for growth curves and fractal scaling (PDF)

AUTHOR INFORMATION

Corresponding Author

Lei Wu — Department of Civil and Environmental Engineering, Ohio University, Athens, Ohio 45701, United States; orcid.org/0000-0002-2781-7251; Phone: (740) 593-4771; Email: wul@ohio.edu

Authors

Christian Bentum Hammond – Department of Civil and Environmental Engineering, Ohio University, Athens, Ohio 45701, United States

Abolfazl Faeli Qadikolae — Department of Chemical and Biomolecular Engineering, Ohio University, Athens, Ohio 45701, United States; oorcid.org/0000-0002-6555-8895

Mohammadreza Aghaaminiha – Department of Chemical and Biomolecular Engineering, Ohio University, Athens, Ohio 45701, United States

Sumit Sharma — Department of Chemical and Biomolecular Engineering, Ohio University, Athens, Ohio 45701, United States; ⊚ orcid.org/0000-0003-3138-5487

Complete contact information is available at: https://pubs.acs.org/10.1021/acs.langmuir.4c01216

Notes

The authors declare no competing financial interest.

ACKNOWLEDGMENTS

L.W. acknowledges the support of the Science Foundation (NSF, grant 1836905). S.S. acknowledges the NSF CAREER grant 2046095 for supporting this work. Computational resources were provided by the Ohio Supercomputer Center and the National Science Foundation ACCESS grant DMR190005.

REFERENCES

- (1) Boyle, K.; Örmeci, B. Microplastics and nanoplastics in the freshwater and terrestrial environment: a review. *Water* **2020**, *12* (9), 2633.
- (2) Alimi, O. S.; Farner Budarz, J.; Hernandez, L. M.; Tufenkji, N. Microplastics and nanoplastics in aquatic environments: aggregation, deposition, and enhanced contaminant transport. *Environ. Sci. Technol.* **2018**, 52 (4), 1704–1724.
- (3) Allen, S.; Allen, D.; Karbalaei, S.; Maselli, V.; Walker, T. R. Micro (nano) plastics sources, fate, and effects: What we know after ten years of research. *Journal of Hazardous Materials Advances* **2022**, 6, No. 100057.
- (4) Sun, H.; Jiao, R.; Wang, D. The difference of aggregation mechanism between microplastics and nanoplastics: Role of Brownian motion and structural layer force. *Environ. Pollut.* **2021**, 268, No. 115942.
- (5) Jiao, R.; Sun, H.; Xu, S.; He, Y.; Xu, H.; Wang, D. Aggregation, settling characteristics and destabilization mechanisms of nanoparticles under different conditions. *Science of The Total Environment* **2022**, 827, No. 154228.
- (6) Jarvis, P.; Jefferson, B.; Parsons, S. A. Measuring floc structural characteristics. *Reviews in Environmental Science and Bio/Technology* **2005**, *4*, 1–18.
- (7) Witten, T. A.; Sander, L. M. Diffusion-limited aggregation. *Phys. Rev. B* **1983**, 27 (9), 5686.
- (8) Ball, R.; Weitz, D.; Witten, T.; Leyvraz, F. Universal kinetics in reaction-limited aggregation. *Physical review letters* **1987**, 58 (3), 274.

- (9) Weitz, D.; Huang, J.; Lin, M.; Sung, J. Limits of the fractal dimension for irreversible kinetic aggregation of gold colloids. *Physical review letters* **1985**, 54 (13), 1416.
- (10) Lin, M.; Lindsay, H. M.; Weitz, D.; Ball, R.; Klein, R.; Meakin, P. Universality in colloid aggregation. *Nature* **1989**, 339 (6223), 360.
- (11) Bushell, G.; Yan, Y.; Woodfield, D.; Raper, J.; Amal, R. On techniques for the measurement of the mass fractal dimension of aggregates. *Adv. Colloid Interface Sci.* **2002**, 95 (1), 1–50.
- (12) Praetorius, A.; Labille, J.; Scheringer, M.; Thill, A.; Hungerbühler, K.; Bottero, J.-Y. Heteroaggregation of titanium dioxide nanoparticles with model natural colloids under environmentally relevant conditions. *Environ. Sci. Technol.* **2014**, *48* (18), 10690–10698.
- (13) Yi, P.; Pignatello, J. J.; Uchimiya, M.; White, J. C. Heteroaggregation of cerium oxide nanoparticles and nanoparticles of pyrolyzed biomass. *Environ. Sci. Technol.* **2015**, 49 (22), 13294–13303.
- (14) Labille, J.; Harns, C.; Bottero, J.-Y.; Brant, J. Heteroaggregation of titanium dioxide nanoparticles with natural clay colloids. *Environ. Sci. Technol.* **2015**, 49 (11), 6608–6616.
- (15) Zhao, J.; Liu, F.; Wang, Z.; Cao, X.; Xing, B. Heteroaggregation of graphene oxide with minerals in aqueous phase. *Environ. Sci. Technol.* **2015**, 49 (5), 2849–2857.
- (16) Huynh, K. A.; McCaffery, J. M.; Chen, K. L. Heteroaggregation of multiwalled carbon nanotubes and hematite nanoparticles: rates and mechanisms. *Environ. Sci. Technol.* **2012**, *46* (11), 5912–5920.
- (17) Feng, Y.; Liu, X.; Huynh, K. A.; McCaffery, J. M.; Mao, L.; Gao, S.; Chen, K. L. Heteroaggregation of graphene oxide with nanometerand micrometer-sized hematite colloids: influence on nanohybrid aggregation and microparticle sedimentation. *Environ. Sci. Technol.* 2017, 51 (12), 6821–6828.
- (18) Davies, S. C.; King, J. R.; Wattis, J. A. The Smoluchowski coagulation equations with continuous injection. *Journal of Physics A: Mathematical and General* **1999**, 32 (44), 7745.
- (19) Frenklach, M. Dynamics of discrete distribution for Smoluchowski coagulation model. *J. Colloid Interface Sci.* **1985**, *108* (1), 237–242
- (20) Wang, X.; Bolan, N.; Tsang, D. C.; Sarkar, B.; Bradney, L.; Li, Y. A review of microplastics aggregation in aquatic environment: Influence factors, analytical methods, and environmental implications. *Journal of Hazardous Materials* **2021**, *402*, No. 123496.
- (21) Gentile, L.; Wang, T.; Tunlid, A.; Olsson, U.; Persson, P. Ferrihydrite nanoparticle aggregation induced by dissolved organic matter. *J. Phys. Chem. A* **2018**, *122* (38), 7730–7738.
- (22) Vikesland, P. J.; Rebodos, R.; Bottero, J.; Rose, J.; Masion, A. Aggregation and sedimentation of magnetite nanoparticle clusters. *Environmental Science: Nano* **2016**, *3* (3), 567–577.
- (23) Demangeat, E.; Pédrot, M.; Dia, A.; Bouhnik-le-Coz, M.; Grasset, F.; Hanna, K.; Kamagate, M.; Cabello-Hurtado, F. Colloidal and chemical stabilities of iron oxide nanoparticles in aqueous solutions: the interplay of structural, chemical and environmental drivers. *Environmental Science: Nano* **2018**, *5* (4), 992–1001.
- (24) Meng, Z.; Hashmi, S. M.; Elimelech, M. Aggregation rate and fractal dimension of fullerene nanoparticles via simultaneous multiangle static and dynamic light scattering measurement. *J. Colloid Interface Sci.* **2013**, 392, 27–33.
- (25) Gambinossi, F.; Mylon, S. E.; Ferri, J. K. Aggregation kinetics and colloidal stability of functionalized nanoparticles. *Advances in colloid and interface science* **2015**, 222, 332–349.
- (26) Liu, J.; Wang, Z.; Sheng, A.; Liu, F.; Qin, F.; Wang, Z. L. In situ observation of hematite nanoparticle aggregates using liquid cell transmission electron microscopy. *Environ. Sci. Technol.* **2016**, *S0* (11), 5606–5613.
- (27) Fernando, I.; Zhou, Y. Impact of pH on the stability, dissolution and aggregation kinetics of silver nanoparticles. *Chemosphere* **2019**, *216*, 297–305.
- (28) Kim, B. H.; Yang, J.; Lee, D.; Choi, B. K.; Hyeon, T.; Park, J. Liquid-phase transmission electron microscopy for studying colloidal inorganic nanoparticles. *Adv. Mater.* **2018**, *30* (4), No. 1703316.

- (29) Sharma, V. K.; Ma, X.; Guo, B.; Zhang, K. Environmental factors-mediated behavior of microplastics and nanoplastics in water: a review. *Chemosphere* **2021**, *271*, No. 129597.
- (30) Wan, J.-K.; Chu, W.-L.; Kok, Y.-Y.; Lee, C.-S. Distribution of microplastics and nanoplastics in aquatic ecosystems and their impacts on aquatic organisms, with emphasis on microalgae. *Reviews of Environmental Contamination and Toxicology Volume* 246 **2018**, 246, 133–158.
- (31) Gmachowski, L. Mass-radius relation for fractal aggregates of polydisperse particles. *Colloids Surf., A* **2003**, 224 (1-3), 45-52.
- (32) Bushell, G.; Amal, R. Measurement of fractal aggregates of polydisperse particles using small-angle light scattering. *J. Colloid Interface Sci.* **2000**, 221 (2), 186–194.
- (33) Goudeli, E.; Eggersdorfer, M. L.; Pratsinis, S. E. Coagulation of agglomerates consisting of polydisperse primary particles. *Langmuir* **2016**, 32 (36), 9276–9285.
- (34) Sorensen, C.; Wang, G. Size distribution effect on the power law regime of the structure factor of fractal aggregates. *Phys. Rev. E* **1999**, *60* (6), 7143.
- (35) Bushell, G.; Amal, R.; Raper, J. The effect of a bimodal primary particle size distribution on scattering from hematite aggregates. *Physica A: Statistical Mechanics and its Applications* **1996**, 233 (3–4), 859–866.
- (36) Eggersdorfer, M. L.; Pratsinis, S. E. The structure of agglomerates consisting of polydisperse particles. *Aerosol Sci. Technol.* **2012**, *46* (3), 347–353.
- (37) Bushell, G.; Amal, R. Fractal aggregates of polydisperse particles. *J. Colloid Interface Sci.* **1998**, 205 (2), 459–469.
- (38) Tence, M.; Chevalier, J.; Jullien, R. On the measurement of the fractal dimension of aggregated particles by electron microscopy: Experimental method, corrections and comparison with numerical models. *J. Phys.* (*Paris*) **1986**, 47 (11), 1989–1998.
- (39) Li, C.; Liu, L.; Zhang, Z.; Zhang, D.; Yi, S.; Yang, H.; Fan, Z. Anisotropy in Near-Spherical Colloidal Nanoparticles. *ACS Nano* **2023**, *17* (18), 17873–17883.
- (40) Singh, A.; Khatun, S.; Gupta, A. N. Anisotropy versus fluctuations in the fractal self-assembly of gold nanoparticles. *Soft Matter* **2020**, *16* (33), 7778–7788.
- (41) Heinson, W.; Sorensen, C.; Chakrabarti, A. Does shape anisotropy control the fractal dimension in diffusion-limited cluster-cluster aggregation? *Aerosol Sci. Technol.* **2010**, 44 (12), i—iv.
- (42) Kim, I.; Taghavy, A.; DiCarlo, D.; Huh, C. Aggregation of silica nanoparticles and its impact on particle mobility under high-salinity conditions. *J. Pet. Sci. Eng.* **2015**, *133*, 376–383.
- (43) Lee, C.-H.; Fang, J. K.-H. Effects of temperature and particle concentration on aggregation of nanoplastics in freshwater and seawater. *Sci. Total Environ.* **2022**, *817*, No. 152562.
- (44) Shupe, H. J.; Boenisch, K. M.; Harper, B. J.; Brander, S. M.; Harper, S. L. Effect of nanoplastic type and surface chemistry on particle agglomeration over a salinity gradient. *Environmental toxicology and chemistry* **2021**, 40 (7), 1820–1826.
- (45) Li, Y.; Girard, M.; Shen, M.; Millan, J. A.; Olvera de la Cruz, M. Strong attractions and repulsions mediated by monovalent salts. *Proc. Natl. Acad. Sci. U. S. A.* **2017**, *114* (45), 11838–11843.
- (46) Hammond, C. B.; Aghaaminiha, M.; Sharma, S.; Shen, C.; Chen, H.; Wu, L. Mesoscale Aggregation of Sulfur-Rich Asphaltenes: In Situ Microscopy and Coarse-Grained Molecular Simulation. *Langmuir* **2022**, 38 (22), 6896–6910.
- (47) Xu, Y.; Ou, Q.; Wang, X.; Hou, F.; Li, P.; van der Hoek, J. P.; Liu, G. Assessing the Mass Concentration of Microplastics and Nanoplastics in Wastewater Treatment Plants by Pyrolysis Gas Chromatography—Mass Spectrometry. *Environ. Sci. Technol.* **2023**, *57* (8), 3114–3123.
- (48) Painter, H.; Viney, M. Composition of a domestic sewage. *Journal of Biochemical and Microbiological Technology and Engineering* **1959**, 1 (2), 143–162.
- (49) Lin, M.; Lindsay, H. M.; Weitz, D.; Ball, R.; Klein, R.; Meakin, P. Universality in colloid aggregation. *Nature* **1989**, 339 (6223), 360–362.
- (50) Wu, L.; Ortiz, C. P.; Jerolmack, D. J. Aggregation of elongated colloids in water. *Langmuir* **2017**, 33 (2), 622–629.

- (51) Heinson, W.; Sorensen, C.; Chakrabarti, A. A three parameter description of the structure of diffusion limited cluster fractal aggregates. *J. Colloid Interface Sci.* **2012**, 375 (1), 65–69.
- (52) Khan, P.; Goel, G. Martini Coarse-Grained Model for Clay—Polymer Nanocomposites. *J. Phys. Chem. B* **2019**, 123 (42), 9011–9023.
- (53) Mohan, K. K.; Reed, M. G.; Fogler, H. S. Formation damage in smectitic sandstones by high ionic strength brines. *Colloids Surf., A* 1999, 154 (3), 249–257.
- (54) Reig, M.; Casas, S.; Aladjem, C.; Valderrama, C.; Gibert, O.; Valero, F.; Centeno, C. M.; Larrotcha, E.; Cortina, J. L. Concentration of NaCl from seawater reverse osmosis brines for the chlor-alkali industry by electrodialysis. *Desalination* **2014**, 342, 107–117.
- (55) Sholl, D. S.; Skodje, R. T. Late-stage coarsening of adlayers by dynamic cluster coalescence. *Physica A: Statistical Mechanics and its Applications* **1996**, 231 (4), 631–647.
- (56) Woehl, T. J.; Park, C.; Evans, J. E.; Arslan, I.; Ristenpart, W. D.; Browning, N. D. Direct observation of aggregative nanoparticle growth: Kinetic modeling of the size distribution and growth rate. *Nano Lett.* **2014**, *14* (1), 373–378.
- (57) Carpineti, M.; Ferri, F.; Giglio, M.; Paganini, E.; Perini, U. Salt-induced fast aggregation of polystyrene latex. *Phys. Rev. A* **1990**, 42 (12), 7347.
- (58) Stankiewicz, J.; Vílchez, M. A. C.; Alvarez, R. H. Two-dimensional aggregation of polystyrene latex particles. *Phys. Rev. E* **1993**, 47 (4), 2663.
- (59) Asnaghi, D.; Carpineti, M.; Giglio, M.; Sozzi, M. Coagulation kinetics and aggregate morphology in the intermediate regimes between diffusion-limited and reaction-limited cluster aggregation. *Phys. Rev. A* **1992**, *45* (2), 1018.
- (60) Ehrl, L.; Soos, M.; Lattuada, M. Generation and geometrical analysis of dense clusters with variable fractal dimension. *J. Phys. Chem. B* **2009**, *113* (31), 10587–10599.
- (61) Melas, A. D.; Isella, L.; Konstandopoulos, A. G.; Drossinos, Y. Morphology and mobility of synthetic colloidal aggregates. *J. Colloid Interface Sci.* **2014**, *417*, 27–36.
- (62) Li, Y.; Girard, M.; Shen, M.; Millan, J. A.; Olvera de la Cruz, M. Strong Attractions and Repulsions Mediated by Monovalent Salts. *Proc. Nat. Acad. Sci. U. S. A.* **2017**, *114* (45), 11838–11843.